3-1-2023

Machine-learning-aided design optimization of internal flow channel cross-sections

Saeel S. Pai
pai15@purdue.edu

Justin Weibel
jaweibel@purdue.edu

Pai, Saeel S. and Weibel, Justin, "Machine-learning-aided design optimization of internal flow channel cross-sections" (2023). *CTRC Research Publications.* Paper 397.
http://dx.doi.org/https://doi.org/10.1016/j.ijheatmasstransfer.2022.123118

Machine-Learning-Aided Design Optimization of Internal Flow Channel Cross-Sections

Saeel S. Pai, Justin A. Weibel

School of Mechanical Engineering, Purdue University

West Lafayette, IN 47906, USA

E-mail addresses: pai15@purdue.edu (Saeel S. Pai), jaweibel@purdue.edu (Justin A. Weibel)

Abstract

The design optimization of various thermal management components such as cold plates, heat sinks, and heat exchangers relies on accurate prediction of flow heat transfer and pressure drop. During the iterative design process, the heat transfer and pressure drop is typically either computed numerically or obtained using geometry-specific correlations for Nusselt number and friction factor. Numerical approaches are accurate for evaluation of a single design but become computationally expensive if many design iterations are required (such as during formal optimization processes). Correlation-based approaches restrict the design space to a specific set of geometries for which correlations are available. Surrogate models for the Nusselt number and friction factor, which are more universally applicable to all geometries than traditional correlations, would enable flexible and computationally inexpensive design optimization. The current work develops machine-learning-based surrogate models for predicting the Nusselt number and friction factor under fully developed internal flow in channels of arbitrary cross section and demonstrates use of these models for optimization of the cross-sectional channel shape. The predictive performance and generality of the machine learning surrogate models is first verified on various shapes outside the training dataset, and then the models are used in the design optimization of flow cross sections based on performance metrics that weigh both heat transfer and pressure drop. The optimization process leads to novel shapes outside the training data, and so numerical simulations are carried out on these optimized shapes to compare with the surrogate model predictions and show their performance is at least as good as that of shapes with known correlations available. A three-lobed shape was found to reduce friction factor, whereas a pentagon with rounded corners and an ice cream cone-shaped duct, both found using different performance metrics. Although the ML model predictions lose accuracy outside the training set for these novel shapes, the

predictions follow the correct trends with parametric variations of the shape and therefore successfully direct the search toward optimized shapes.

Keywords: fully developed, internal, single-phase flow, Nusselt number, friction factor, machine learning, artificial neural network, optimization

Nomenclature

A	area of channel cross section, m^2
ANN	artificial neural network
c_p	specific heat capacity, J/(kg K)
D_h	hydraulic diameter, m
dP/dz	flow pressure gradient
f	Fanning friction factor ($(dP/dz)D_h/(2\rho v^2)$)
f_i ($\boldsymbol{x}$)	objective function for optimization
$g(\boldsymbol{x})$	inequality constraint
h	heat transfer coefficient, W/(m^2 K)
$h(\boldsymbol{x})$	equality constraint
j	Colburn j-factor ($Nu/(RePr^{1/3})$)
k	thermal conductivity, W/(m K)
MAE	mean absolute error
MSE	mean squared error
ML	machine learning
Nu	Nusselt number (hD_h/k)
Nu_{H1}	Nusselt number for $H1$ boundary condition
Nu_{H2}	Nusselt number for $H2$ boundary condition
P	wetted perimeter
Pr	Prandtl number ($\mu c_p/k$)
Re	Reynolds number
v	average flow velocity, m/s
μ	fluid dynamic viscosity, N s/m^2
ρ	density of fluid, kg/m^3

1. Introduction

The design and optimization of heat sinks, cold plates, and heat exchangers relies on accurate prediction of Nusselt number and friction factor for internal flow through a wide variety of heat transfer surfaces. Correlations for these geometry-dependent non-dimensional numbers are available for commonly encountered flow geometries, obtained either though analytical solutions, numerical solutions, or physical experiments, resulting in different correlations for each specific geometry. It is difficult to make use of this large number of disconnected Nusselt number and friction factor correlations in the process of design optimization of heat transfer surfaces. Thus, there is a need collapse this catalogue of correlations for all commonly encountered heat transfer surfaces into more a generalized and readily accessible form.

In recent years, instead of fitting functions to experimental and simulation data to develop correlations, machine learning (ML) methods have been successfully used to create surrogate models across various scientific fields. These methods allow the models to capture highly non-linear transport phenomena without having to assume a functional form for a correlation. The use of data-driven machine learning approaches has influenced various fields including medicine, manufacturing, energy, transportation, software development, agriculture, and even artistic creations [1]. Most notable, machine learning has fueled major advances in computer vision applications, has leading to improvements in non-destructive testing, medical imaging, autonomous vehicles, and geomatics, to name a few. Within traditional mechanical engineering disciplines, the use of ML techniques has matured in areas such as solid and fracture mechanics [2,3], fluid dynamics and turbulence modeling [4,5], and energy systems analysis [6–10]. In comparison, the more recent adoption of ML methods for heat and mass transfer analyses, as reviewed below, is less widely explored.

In the area of convective transport, there have been a few studies on developing ML-based surrogate models for predicting the heat transfer and pressure drop characteristics for certain configurations of nanofluid flows [11–13], boiling/condensing two-phase flows [14–18], and single-phase flows in general [19–27]. However, prior studies that develop surrogate models for single-phase convection focus on capturing the parametric variations for very specific flow geometries. For example: Parrales et al. [19] and Beigzadeh and Rahimi [20] trained artificial neural networks (ANNs) to predict the Nusselt number and friction factor for flow in helical tubes; Xie et al. [21,22] trained ANNs to predict the heat transport and fluid flow relations for shell-and-tube and fin-and-tube heat exchangers; Beigzadeh et al. [23] and Ostenak [24] trained

ANNs to predict the Nusselt number and friction factor for interrupted plate fins and circular pin-fins respectively; and Chokphoemphun et al. [25], Islamoglu and Kurt [26], and Kwon et al. [27] developed ANN and random-forest-based surrogate models for predicting the heat transfer and fluid flow parameters for grooved, corrugated, and ribbed array channel geometries, respectively. More universal surrogate models are not available to predict the Nusselt number and friction factor for a wide variety of flow geometries. Such surrogate models, applicable across differing flow geometries, would allow bypassing of the flow and heat transfer simulations that are otherwise required in the design optimization of thermal management components. Even for the simplest case of constant cross-section flow channels, the focus of the current work, universal surrogate correlations which predict the heat transfer and fluid flow properties for a wide range of cross-sections do not exist. Hence, the process of optimizing the constant cross-section flow channel for a given design metric requires the use of numerical simulations, owing to the geometry specific nature of existing correlations.

In this work, we develop machine-learning-based surrogate models for internal flow through channels of arbitrary constant cross-section, which are then demonstrated for use in design optimization of the cross-sectional shape. A surrogate model for predicting the friction factor (*fRe*) and two models for predicting the Nusselt number under both *H*1 and *H*2 boundary conditions are developed. *H*1 and *H*2 are essentially two different types of constant flux boundary conditions; in the *H*1 boundary condition, the heat flux is uniform along the flow direction and the wall temperature is uniform along the perimeter of the duct cross section, while in the *H*2 boundary condition, the heat flux is constant along both. These ML models are trained on existing data and correlations compiled for all available constant cross section geometries of interest. The design optimization is formulated to maximize design metrics aimed to increase the heat transfer rate and simultaneously reduce the pressure drop in the channel. The following sections introduce the developed ML models, verify their prediction accuracy on geometries outside the training data set, and then employ the model in the design optimization of constant cross section internal flow geometries.

2. Machine-Learning-Based Surrogate Model

2.1. Model Development

An artificial neural network (ANN) ML architecture is chosen as it is a mature approach that has been successfully used in various applications. An ANN is a computing system inspired by the biological neural networks in animal brains. It is a directed acyclic graph which

consists of nodes (or artificial neurons) which are connected to each other. Connections between the neurons transmit information from one neuron to another. Every neuron processes the information it receives and then relays this processed information to downstream neurons to which it is connected. Figure 1 shows a schematic diagram of an ANN along with the inputs and outputs specific to this work. The nodes in an ANN are typically arranged in the form of layers as shown. Information enters the network from the layer of nodes on the far left, called the input layer, and the output layer of nodes on the far right gives the final prediction based on the input information. The layers in between the input and the output layers are called the hidden layers. ANNs are powerful function approximators, and it has been shown that they (under certain conditions) can be used to approximate any continuous function [28]. The power of an ANN lies in its ability to extract underlying rules governing an input dataset and then make predictions for new data based on the rules learned. In the current ML model [29], the input layer encodes the geometric information of the flow channel cross-section as a vector (Figure 1); the single output node represents the predicted quantity (Nu_{H1}, Nu_{H2}, or fRe). The ANN development, including justification for the choice of the rectified linear unit (ReLU) activation function, training data partitioning strategy, hyperparameter tuning process, loss function selection, and ensemble method are summarized below.

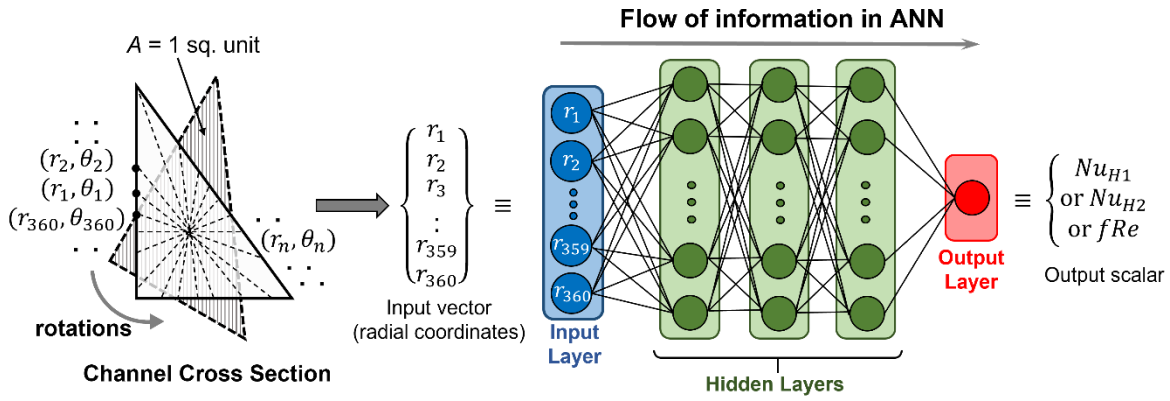

Figure 1. Structure of the ANN used in the prediction of Nusselt number and friction factor for internal flow channel geometries. The channel geometry represented in polar coordinates is given as the input and ANN is trained to predict the Nusselt number or friction factor.

The performance of ML algorithms depends on the amount and quality of training data (in general, more data leads to better training). Nusselt number (Nu_{H1} and Nu_{H2},) and friction factor (typically presented as the product fRe in correlations) data of different constant cross section flow shapes were collected from established literature [30][31]. These flow shapes span a wide range of shape classes (listed in Table 1). Each shape class has parametric variations

such as their aspect ratios and included angles. As *Nu* and *fRe* are non-dimensional, their conversion to heat transfer coefficient '*h*' and pressure drop requires a characteristic length, taken as the hydraulic diameter, $D_h=4A/P$, in the data used. Separate surrogate models are built for Nusselt number under the *H*1 and *H*2 constant heat flux boundary conditions.

To ensure rotational invariance during the training process, several orientations of each distinct shape were used in the training of the ANN [29]. In general, 360 different rotations were considered for each distinct shape, i.e., one for each degree of rotation. However, for many of the shapes, several rotated versions are discarded due to symmetry. For example, for an ellipse or rectangle, only rotations from 1° to 180° were considered, due to a two-fold axis of symmetry. Similarly, a regular polygon with *n* sides has an n-fold axis of symmetry so only rotations from 1° to 360°/*n* (to the nearest degree) are considered. In some other cases, like in the case of trapezoids, rotations were considered at intervals larger than 1° so that total number of data points from this shape do not have undue influence over the dataset. The number of different orientations for each shape generally tries to ensure an equitable distribution of total samples belonging to each distinct shape. The total number of training data samples across all orientations is 70,262 for Nu_{H1}, 55,334 for Nu_{H2} and 94,322 for *fRe*.

Table 1. List of flow cross section shapes in the dataset. The number of available distinct and total shapes across all shape classes are specified for Nu_{H1}, Nu_{H2} and *fRe*.

No	Shape Class of Flow Cross Section	Nu_{H1}		Nu_{H2}		*fRe*	
		Distinct	**Total**	**Distinct**	**Total**	**Distinct**	**Total**
1	Isosceles Triangle	37	6660	37	6660	37	6660
2	Right Triangle	20	7200	20	7200	20	7200
3	Corrugated Circle	18	553	18	553	18	553
4	Regular Polygons	18	751	18	751	18	751
5	Trapezoid	228	8208	120	4320	228	8208
6	Rhombus	35	6300	35	6300	35	6300
7	Segment of a Circle	71	6390	71	6390	71	6390
8	Equilateral Triangle (Rounded Corners)	3	840	3	840	3	840
9	Sinusoid	40	7200	40	7200	40	7200
10	Ellipse	20	3600	20	3600	20	3600
11	Rectangle	19	3420	19	3420	19	3420
12	Sector of a Circle	35	6300	35	6300	35	6300
13	Quadrilaterals	4	1440	4	1440	4	1440
14	Cardioid	1	360	1	360	1	360
15	Arbitrary Triangle	35	4200	-	-	28	3360
16	Rectangle (Semicircular Ends)	19	3420	-	-	19	3420

17	Circle (Flat Ends)	19	3420	-	-	19	3420
18	Square (All Indented Corners)	-	-	-	-	50	4500
19	Square (One Indented Corner)	-	-	-	-	12	4320
20	Star	-	-	-	-	22	1980
21	Lens	-	-	-	-	16	2880
22	Rectangle (Two Indented Corners)	-	-	-	-	12	4320
23	Horseshoe	-	-	-	-	5	1800
24	Football	-	-	-	-	3	540
25	Boomerang	-	-	-	-	2	720
26	Elliptic Circle	-	-	-	-	2	720
27	Equilateral Triangle (Indented Corners)	-	-	-	-	2	240
28	Atomic Bunker	-	-	-	-	1	360
29	Kite	-	-	-	-	1	360
30	Symmetric L	-	-	-	-	1	360
31	Asymmetric L	-	-	-	-	1	360
32	Milk Can	-	-	-	-	1	360
33	Parabola	-	-	-	-	1	360
34	Rectangle (Unilateral Circular Ends)	-	-	-	-	1	360
35	Rectangle (Unilateral Elliptical Ends)	-	-	-	-	1	360
Total		**622**	**70,262**	**441**	**55,334**	**749**	**94,322**

Polar coordinates are used to represent the flow cross section shape that is input to the ML model, as shown in the left side of Figure 1. The area of every cross section is normalized to one square unit, and the origin is placed at the center of mass such that any point on the boundary of the geometry can be represented in terms of a (r, θ) tuple. Because the same θ values (viz., 360 linearly spaced values from 1° to 360°) are used for all the geometries in the dataset, they can be excluded from the input, leaving only the radial coordinates of each boundary point as an ordered set. Thus, the input to the ML model is a 1×360 vector of the radial coordinates of the points on the boundary of the input geometry in 1° rotational increments. Note that the angular starting point in the ordered set is made irrelevant due to the training on many different orientations of the same shape to ensure rotational invariance.

The Huber loss function was chosen for training the ML models as it was found to perform better than other commonly used loss functions like the mean squared error (MSE) or mean absolute error (MAE) loss functions. Huber, which is quadratic for small errors and linear for larger errors, is less sensitive to outliers than MSE and differentiable at zero unlike MAE. The number of hidden layers and the number of nodes per layer in the ANN were optimized through

a grid search and 5-fold cross validation process. The complete dataset was first randomly split into train and test datasets (70:30 ratio) and a preliminary grid search was performed by varying the number of layers from 1 to 5 and number of nodes in each layer from 10 to 250. At this stage of the training, the number of nodes in each layer were kept equal. For all three models, 3 hidden layers gave the best compromise between the training time and the prediction accuracy on the testing set. Next, the optimal numbers of nodes in each of the 3 layers were found by first doing a grid search on a random train-test (70-30) split of the data, choosing the top few high-performing combinations of number of nodes (based on goodness of fit values), and then doing a 5-fold cross validation with each of those combinations. In general, k-fold cross validation is a technique to assess the skill of ML models. In this method, the dataset is randomly divided into k groups, or folds, of approximately equal size, where one fold is treated as a testing set and the model is trained on the remaining k − 1 folds. This process of training and testing is repeated on every split in a cyclic manner to obtain the mean prediction metric. Three-layer ANNs were found to have a good bias–variance trade-off for all three models (Nu_{H1}, Nu_{H2}, and *fRe*). The optimal numbers of nodes in the 3 layers of the ANNs were found to be 250-100-50 for the Nu_{H2} data and 150-150-150 for the *fRe* data. For the Nu_{H1} data, ANNs with 150-150-25 and 150-200-50 both performed similarly.

The results supporting the choice of the hyperparameters are discussed in the Supplemental Material section 1. The Nu_{H1}, Nu_{H2} and *fRe* models with the above hyperparameters, trained on 70% of the data, have R^2 values of 0.99, 0.99 and 0.935 on the 30% test data, which consists of unseen data but belonging to the shape classes defined in Table 1. Because heat is transferred in ducts of all shapes via the same physical processes, it is fair to assume that all the Nusselt numbers for different ducts come from the same underlying distribution. Thus, hyperparameters that are optimized using 70% of the data would also be optimal for models trained on the entire dataset. The same argument holds for friction factor. This method of tuning hyperparameter on parts of the dataset, and then using those hyperparameters to refit the final model on the entire dataset is a commonly used ML technique to ensure utilization of all the currently available data to make models for prediction of new, unseen, future cases.

Ensemble ML models are known to perform better than any of the constituting individual models, and they also improve the stability of the predictions by reducing variance. Bootstrap aggregating, commonly known as bagging, is an ensemble technique that was used to improve the performance of the *fRe* and *Nu* models. Given a training dataset S of size n, bagging generates m new datasets S_i (i=1, 2..., m) of size n by sampling uniformly from S but with

replacement. Thus, each datapoint in S may appear repeated times or not at all in any particular S_i. For a large n, any S_i is expected to have around 63.2% of the unique examples from S. In this work, a value of m=20 has been used for all three models. The final *fRe* surrogate model is an ensemble of 20 ANNs with 150-150-150 nodes in the hidden layers, the Nu_{H2} model is an ensemble of 20 ANNs with 250-100-50 nodes in the hidden layers, and the Nu_{H1} model is an ensemble of 10 ANNs with 150-150-25 nodes and 10 ANNs with 150-200-50 nodes in the hidden layers.

All the models have been trained using Keras in TensorFlow on Google Colaboratory. The optimization of weights was carried out using the Adam optimization algorithm, for 300 epochs, by which time the model predictions had converged [29]. Because the training data sets were randomly selected from the main dataset, it is assumed that both these datasets come from similar distributions, and hence, these sets of hyperparameters will also give a good performance (i.e., no over/under fitting) when trained on the entire dataset. Therefore, models with the hyperparameters mentioned above were trained on the entire dataset. The ML models are published as a tool available on nanoHUB.org [32], and recommended for use as surrogate correlations within training dataset.

The performance of the models is depicted in Figure 2. The performance statistics are calculated on a set which consists of all the distinct shapes in the original dataset. For each distinct shape, the *Nu* and *fRe* values are calculated by averaging out the model predictions across 360 different rotational orientations (one per degree of rotation). It is found that for some shapes, at extreme aspect ratios, the individual predictions at some orientations have increased error, but when the average of each individual prediction across several rotational orientations is taken as final predicted value of the output (*Nu* or *fRe*), the error in the prediction is reduced significantly [15]. The plot on the left of Figure 2 shows the mean percentage errors between the three ML surrogate model final predictions and the training data over the 14 shape classes which are common across the datasets. The percentage error on each shape is less than 5%, except for the first two classes (isosceles and right triangles) for which the Nu_{H2} model gives higher error. The box plot on the right shows the percentage error averaged across all the shapes in the respective datasets. The diamond markers indicate the shape classes that are outliers in the box and whisker plots. The mean percentage error is 0.70% for the *fRe* model, 1.24% for the Nu_{H1} model, and 2.84% for the Nu_{H2} model. A summary of the model performance statistics is given in Table 2. The table shows the absolute and percentage mean errors, and the number and percentage of outliers. For all three models, the mean percentage errors are less than 3%,

and the percentage of outliers is around 10%. Thus, the models perform satisfactorily on all the different shapes in the dataset drawn from existing correlations.

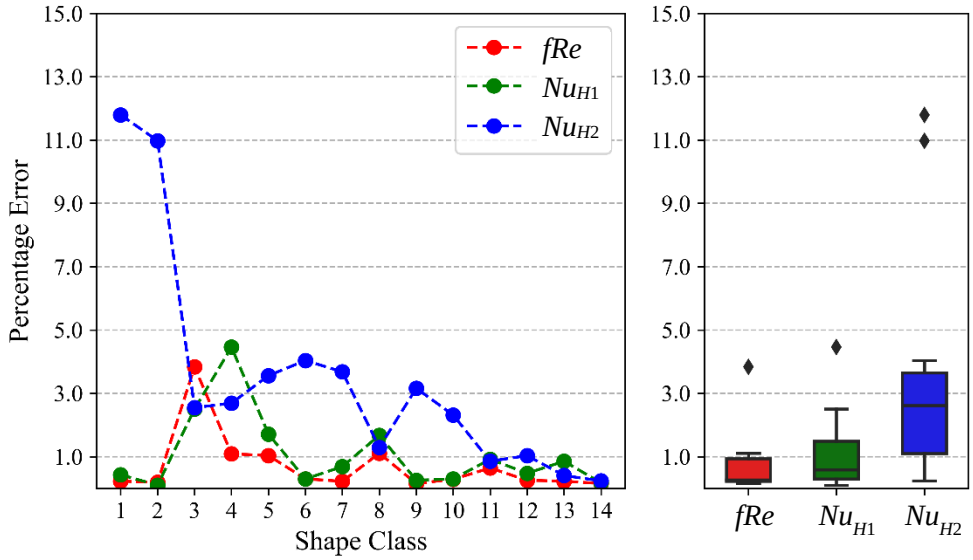

Figure 2. Error plots for the *fRe* and *Nu* models: (left) percentage error in the model predictions for each of the 14 shape classes common to the *fRe*, Nu_{H1}, and Nu_{H2} models, indexed as per the list in Table 1; (right) box plot showing the the percentage error averaged across all the shapes in the *fRe*, Nu_{H1}, and Nu_{H2} datasets.

Table 2. Summary of error statistics in the predictions of Nu_{H1}, Nu_{H2} and *fRe* by the surrogate ML models on the respective training datasets from available correlations.

	Nu_{H1}	Nu_{H2}	*fRe*
Mean Absolute Error	0.0531	0.0297	0.1083
Mean Percentage Error	1.24	2.84	0.70
Number of Outliers	66	44	63
Percentage of Outliers	10.76	9.97	8.52

2.2. Model Predictions on Shapes Outside the Primary Training Shape Classes

To assess the ML model generality in prediction of *Nu* and *fRe* outside the dataset of existing primary shape classes, several different shapes were generated. Primary shape classes have been defined as those classes in Table 1 which contribute more than one distinct case to the training data. The ML model prediction on these shapes is compared to *Nu* and *fRe* values obtained by carrying out numerical simulations of fully developed internal flow through channels having these cross sections. Predictions are performed for parametric variations of a

half lens, half parabola, and parabola (see the shape cross sections and definition of the varied geometric parameters in the inset sketched within Figure 3).

The numerical finite volume simulations (ANSYS Fluent) are carried out with water as the working fluid. Flow channels with 1-2 mm hydraulic diameters and channel lengths of 600 mm are used (sufficiently long to confirm fully developed flow). Constant fluid properties and a low flow rate to ensure laminar flow (*Re* between 100-500) are maintained. The pressure drop and heat transfer characteristics are extracted from a location in the latter half of the flow channel (at a distance of 500 mm) where developing effects are no longer present, but slightly away from the channel exit to prevent boundary-effects from influencing the results. The Nu_{H1} boundary condition is simulated using a 1 μm-thick shell layer of a highly conducting fictitious material (thermal conductivity of 2×10^4 W/(m K)) with constant wall heat flux boundary condition. The shell conduction layer only allows circumferential conduction of heat, with no conduction along the axial (flow) direction. This configuration ensures that the heat flux applied to the walls is spread uniformly around the channel perimeter to provide a uniform wall temperature over the channel cross section (i.e., a constant wall heat flux along the flow direction and constant wall temperature along the channel perimeter). The Nu_{H2} boundary condition is simulated by simply having a constant wall heat flux boundary condition without any shell conduction layer (i.e., a constant wall heat flux along both the channel flow direction and perimeter). The SIMPLE solution scheme is used with 2nd order pressure and momentum discretization. The convergence criteria are set to 1×10^{-6} for the continuity, velocity, and energy residuals. The simulation meshes, generated using the sweep option along the axis, with an element size of 0.5 mm on the faces and 2 mm along the axis, are found to give mesh-independent results.

Figure 3 compares the ML model predictions of *fRe* (top) and *Nu* (bottom) with values obtained from the finite-volume simulations for parametric variations of the half lens (left), half parabola (center) and parabola (right). For all three shape classes, the *fRe* values from the ML model are very close (often almost overlapping) to the values obtained through finite-volume simulations. The *Nu* values obtained from the ML model are not as accurate, in particular the Nu_{H1} values for the half parabola and the Nu_{H2} values for the half lens.

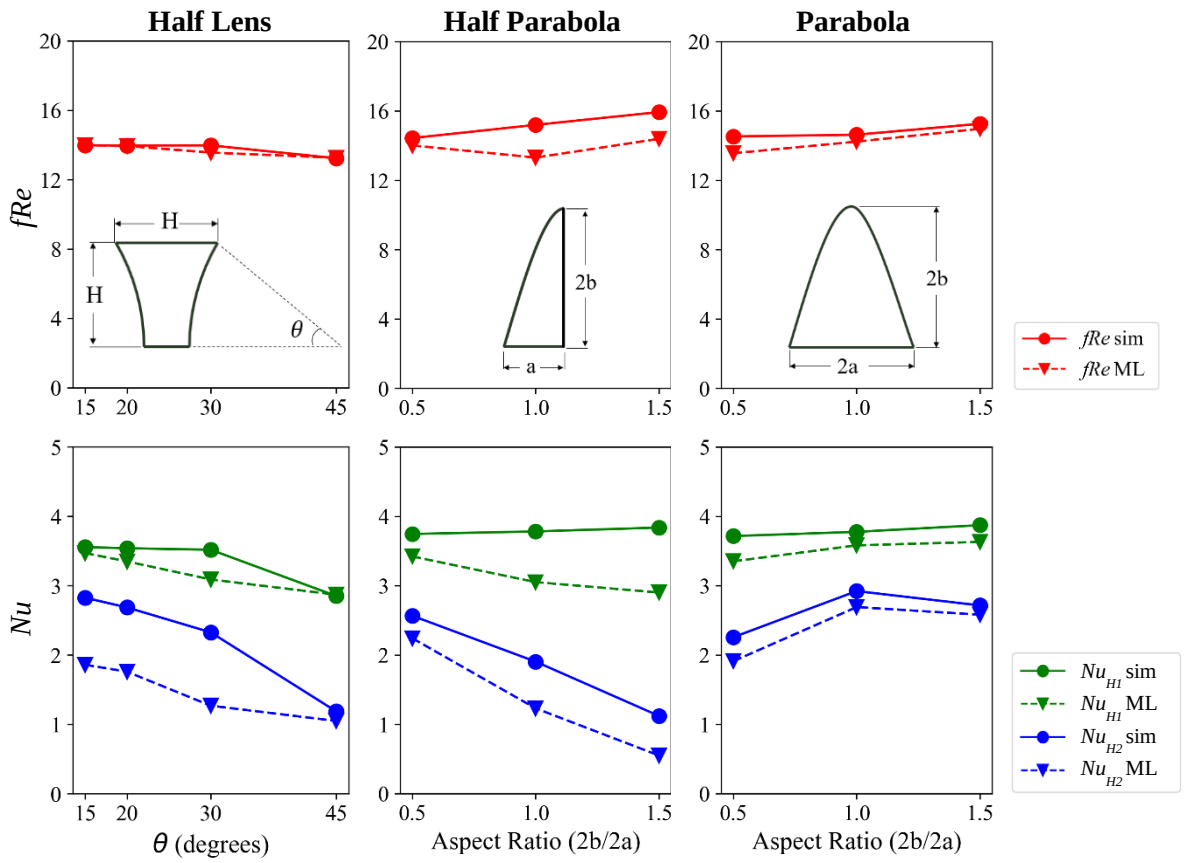

Figure 3. Comparison between numerically simulated and ML-predicted *fRe* and *Nu* values for the new shapes: half lens (left), half parabola (center), and parabola (right).

Overall, the ML models have a mean percentage error of 4%, 10%, and 25% in predicting the *fRe*, Nu_{H1} and Nu_{H2} values of these new shapes, but they capture the trends in the *fRe* and *Nu* values with parametric variations in the shape. For example, even for the half lens shape for which the numerical value of the Nu_{H2} prediction is the least accurate, the ML model predictions follow the correct trend with variation in the included angle. With the intent to use such surrogate ML models in design optimization approach, it is important to predict the correct trends so as to drive shape changes toward the optimal. Once optimized geometries are identified using low-cost surrogate model, it is expected that quantitatively correct values of the pressure drop and heat transfer coefficient would be obtained from numerical simulations or other exact solution methods, especially if the obtained shape belongs to a shape class outside the primary training classes.

3. Design Optimization

3.1. Performance Metric

In convective cooling applications, a high heat transfer coefficient is desired to extract the maximum amount of heat at a given temperature difference, and a lower friction factor to reduce the pressure drop and thereby pumping power. Thus, heat exchanger geometries are often selected using performance metrics that simultaneously consider both the Nusselt number and friction factor; these performance metrics can also serve as objective functions for design optimization. The modified 'area goodness' performance metric that is commonly used in the design of heat exchangers, is selected to form the objective function to optimize the channel cross sectional shape in this work. The area goodness is defined as the ratio of Colburn-j factor and the friction factor (f) as $Nu/(fRePr^{1/3})$. As the Prandtl number is a property of the working fluid, for a given fluid, it is assumed to be constant and hence optimizing the area goodness is equivalent to optimizing *Nu/fRe*. Physically, the area goodness provides a measure of the frontal area required for a heat exchanger to operate at a given design point (viz., flow rate, pressure drop, and total surface area). A lower required frontal area corresponds with a higher area goodness per the formulation of this metric.

3.2. Formulation of the Optimization Problem

The process of optimizing the channel geometry to maximize the performance metric requires a model for prediction of the Nusselt number and the friction factor for the geometries generated. Rather than carrying out computationally expensive numerical simulations at each iteration, the ML-based surrogate models developed in this work are used to predict the Nusselt number and friction factor of the channel cross section shape during the optimization process. The design optimization is carried out by importing the ML-based surrogate models developed using TensorFlow into MATLAB v2020b.

The optimization problem of maximizing *Nu/fRe*, is equivalent to minimizing *-Nu/fRe*. Because optimization methods are typically designed to minimize the value of the objective function, the objective function is written as

$$f_1(\boldsymbol{x}) = -\frac{Nu}{fRe} \tag{1}$$

Similarly, objective functions based on the standalone friction factor and Nusselt number can be respectively written as $f_2(\boldsymbol{x}) = fRe$ and $f_3(\boldsymbol{x}) = -Nu$. These objectives are functions of the flow cross section represented in a polar coordinate system as 360 equiangularly spaced radial points $\boldsymbol{x}$, the same as the 1×360 vector input to the ML surrogate models for predicting the *Nu* and the *fRe* values. For the models to give precise predictions, it is also necessary that the area of the

enclosed geometry is one square unit. If $\boldsymbol{x}$ is an 'n' dimensional vector, the area of the geometry can be approximated as

$$A = \frac{sin\,(d\theta)}{2}(\boldsymbol{x}_1\boldsymbol{x}_2 + \boldsymbol{x}_2\boldsymbol{x}_3 + \ldots + \boldsymbol{x}_n\boldsymbol{x}_1) \tag{2}$$

where for equiangular spaced radial points $\boldsymbol{x}$, $d\theta = 2\pi/n$. Writing this area constraint in the form of equality constraint $h(\boldsymbol{x}) = 0$ yields

$$h(\boldsymbol{x}) = \frac{sin\,(2\pi/n)}{2}(\boldsymbol{x}_1\boldsymbol{x}_2 + \boldsymbol{x}_2\boldsymbol{x}_3 + \ldots + \boldsymbol{x}_n\boldsymbol{x}_1) - 1 \tag{3}$$

For a physical shape, it is necessary that $\boldsymbol{x}_i \geq 0$, and thus the lower bound on $\boldsymbol{x}$ is 0. However, preliminary runs of the several optimization algorithms discussed below showed that the values of $\boldsymbol{x}_i$ were typically confined between 0.2 and 1 (for a perfect circle, all $\boldsymbol{x}_i = 0.5642$ for the area to be one square unit). Thus, for most subsequent optimization processes, the range of $\boldsymbol{x}_i$ was constrained between 0.2 and 1 to reduce the search space and expedite convergence. Therefore, an upper bound is often used to prevent the result from being a completely skewed shape.

As the *Nu* and *fRe* values are obtained from the ML model, functions involving either of these two quantities are non-analytic functions. As analytic derivatives cannot be obtained for functions involving these two quantities, numerical-derivative-based and non-derivative methods have been considered. Four different methods have been employed to optimize the flow cross section: 1) interior point method (IPM); 2) sequential quadratic programming (SQP); 3) genetic algorithm (GA); and 4) Nelder-Mead (NM) simplex. The IPM and SQP are derivative-based methods for which numerical derivatives have been used, while GA and NM are non-derivative methods. The IPM and SQP have been employed using MATLAB's constrained multivariable nonlinear optimizer (*fmincon* function), whereas the NM simplex has been employed using MATLAB's direct search method (*fminsearch* function). The GA has been employed using a code developed at Purdue University (see Acknowledgements)

While the *Nu* and *fRe* ML models take a 1×360 vector input, the number of control points was reduced because 360 were found to generate shapes with fine features highly dissimilar from the training data and therefore beyond the predictive precision of the trained ML models. During the shape optimization, 45 equiangular control points are used to represent the channel geometry. Cubic interpolation is used to generate an interpolated 1×360 vector input to the ML models for predictions of *Nu* and *fRe*. The problem formulation for IPM is given below; The formulations for the other methods are described in the Supplemental Material section S2.

For IPM, the objective function is $f_1(\boldsymbol{x})$ (equation (1)), subject to the bounds $0 \leq \boldsymbol{x}_i \leq 2$, $i = 1, 2\ldots, 45$ and the equality constraint $h(\boldsymbol{x}) = 0$ (equation (3)), as described above. The algorithm was observed to output very wavy shapes, so it was run in a cyclic manner, with cycles of a few hundred iterations each, where a Savitzky-Golay filter with order 2 and frame length 7 was used on the output of each cycle before feeding it back as the initialization for the next cycle. This was found to reduce the propagation and amplification of noise.

Once the optimized cross section shape is obtained via any of the optimization methods, post-processing is performed on this raw shape to obtain a regular (i.e., having some rotational symmetry) shape having similar characteristics. Predictions of the performance of that regular shape (scaled to have an area of 1 square unit) obtained by numerical simulations are then compared to the ML surrogate predictions.

3.3. Results and Discussion on the Design Optimization

The four optimization methods are first applied on the basis of the area goodness metric (with *H*2 boundary condition). The IPM, SQP, and NM simplex were run with different initializations and for different numbers of cycles, and the highest Nu_{H2}/fRe values, along with the corresponding Nu_{H2}, fRe and areas, were noted. Similarly, the GA was run with different input vector lengths and bits per input vector. A detailed discussion of the tabulated results is provided in the Supplemental Material section S3. In summary, it is concluded that the interior point method, with 3 cycles and a normal random initialization performed the best. Therefore, IPM is applied with the friction factor, Nusselt number, and area goodness metrics to identify optimized shapes.

With friction factor (fRe) minimization as the objective function, an optimized geometry is identified by performing several trials with different random initializations. The maximum number of function evaluations per cycle was capped at 1500 after which the Savitzky-Golay filter was applied to smoothen the shape. Cross sectional shapes having a characteristic three-lobed structure obtained from the optimization process have fRe values in the range of 6.60 to 9.20, with an average value of 7.49. Figure 4 (a) uses dashed lines to show a couple of representative output shapes for this objective function. Next, using IPM to maximize the value of Nu_{H2} leads to a regular circular shape with a predicted Nu_{H2} value of 4.36. The circular duct has the highest Nu_{H2} value in the training dataset, so it is expected that the optimization algorithm would converge to this trivial result. On the other hand, optimization of Nu_{H1} tends to two different shapes either a circular shape when randomly initialized or a rectangular shape

when given a rectangular initialization. In the training data, Nu_{H1} values of some rectangles are greater than that of a circular duct, and so one would expect a non-circular optimum, indicating the shape results are local optima.

For the area goodness metrics, the optimal shapes obtained from a random initialization differ with the *H*1 versus *H*2 boundary condition. From several runs with an *H*1 boundary condition, the representative optimized shapes as shown in the dashed lines in Figure 4 (b) are amoeba-like, typically with four to six pseudopodia (most often five). The *H*2 boundary condition yields ice cream cone-like shapes as illustrated in Figure 4 (c). In general, the *Nu/fRe* values for these shapes as predicted by the ML models notably exceed that of circular ducts (e.g., *Nu/fRe* = 0.2725), and hence, these identified shapes are of interest for further inspection with higher fidelity numerical simulation.

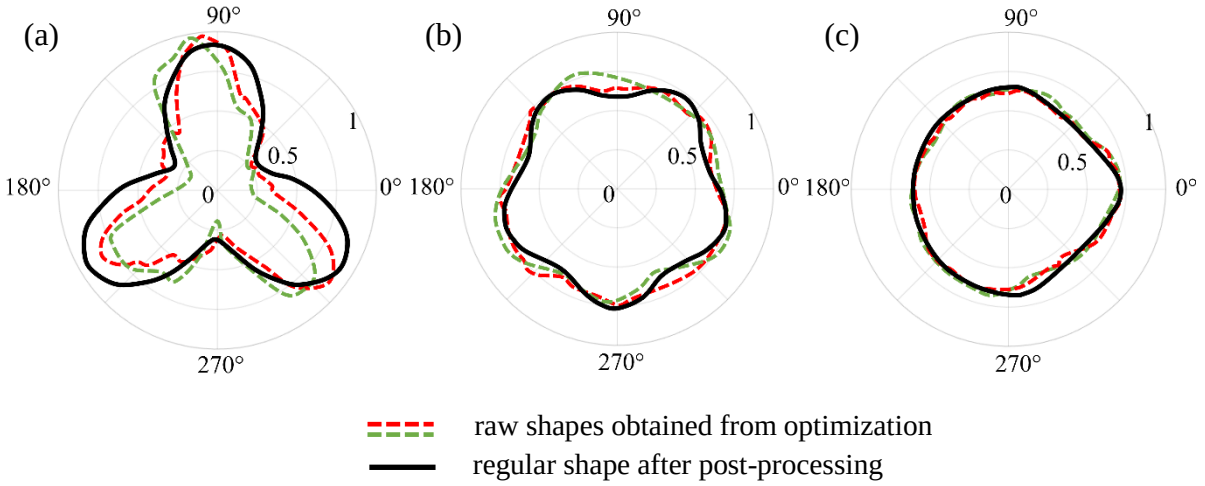

Figure 4. Examples of typical shapes as the raw optimization outputs (dashed lines) overlaid by the post-processed regular geometry (solid black line) when the objective function is: (a) *fRe*, (b) Nu_{H1}/fRe, and (c) Nu_{H2}/fRe.

For better generalizability, the optimized shapes are post-processed (smoothened) to a more regular shape while retaining the key features of the optimized shapes identified from several runs of the optimization algorithm. The regular shapes were created by choosing forms of equations which are known to have the specific characteristics identified in the raw optimized shapes, and then selecting the parameters within these equations to match the raw shapes through a trial-and-error process. The regular shapes are constrained to an area of one square unit. Finite volume simulations are performed on these regular shapes to find the exact values of *Nu* and *fRe*, and these results are compared to the ML models' predictions on those regular

shapes. Figure 4 shows the post-processed regular shape overlaid as a solid black line on the previously discussed raw optimizations for each of the optimization functions. The three-lobed shape is represented using an area-normalized cosine wave superimposed on a circle ($r = 1 + 0.5cos(3\theta)$, $\theta \in [0,2\pi]$), shown in Figure 4 (a). For the amoeba--like shapes with five pseudopodia, shown in Figure 4 (b), the regular form is a pentagon with rounded corners, generated using an area-normalized cosine wave superimposed on a circle ($r = 1 + 0.1cos(5\theta)$, $\theta \in [0,2\pi]$). The regular version of the ice-cream cone-like shape is generated using a semicircle and a cubic spline, as shown in Figure 4 (c). All three optimized shapes lie outside the training shape classes, and hence numerical simulations are carried out to determine the exact values of *Nu* and *fRe*.

These results from numerical simulations and ML model predictions for the raw and regular post-processed shapes for the three metrics are summarized in Table 3. Numerical and ML model predictions on the regular three-lobed sinusoidal shape gave *fRe* values of 9.24 and 14.11, respectively. While this *fRe* value predicted by the numerical simulation is not as low as that predicted by the ML model for the raw shapes during the optimization process, it is still notably lower than the *fRe* value of 16 for a circular channel. On the regular (post-processed) pentagon with rounded corners, numerical simulations and ML model predictions give Nu_{H1}/fRe values of 0.274 and 0.255 respectively, while the regular version of the horizontal ice-cream shaped duct gives Nu_{H2}/fRe values of 0.266 and 0.368 from numerical simulations and ML models respectively. From the last four columns of Table 3, it is generally seen that the *Nu* predictions from the ML models are usually quite accurate, but the *fRe* predictions have higher error. While the ML models capture the trends in parametric variations and steer the design toward more optimal shapes, exact values of *fRe* and *Nu* should be confirmed using numerical simulations.

To assess how the obtained optimized shapes compare against existing shapes in the training set, the performance metric values of the optimized shapes are compared with that of shapes in the training dataset. Figure 6 shows a plot of the Nu_{H2}/fRe as a function of Nu_{H2} for shapes in the training data (blue dots), the raw optimized shapes as predicted by the ML models (red dots), and the post-processed optimized shapes as predicted by numerical simulations (green dots). The Nu_{H2}/fRe values obtained from the ML models on the optimized shapes are seen to be much higher than for any shape in the training data (for a given Nu_{H2}); numerical simulations on the post-processed versions of these shapes pull these Nu_{H2}/fRe values back to the pareto front formed by the training data. This trend was also observed with the Nu_{H1}/fRe

metric. Thus, the new shapes identified by the optimization process are optimal, but their performance does not break though as an outlier beyond the expected pareto front. Nevertheless, using the optimization process, this ML surrogate optimization approach was able to identify novel shapes (otherwise lacking available correlations) which have performance comparable to currently known optimal shapes, if not marginally better. Over the past several decades, this two-dimensional design space has been exhaustively explored, so it is not a surprise that significantly more optimal shapes weren't identified. Rather, the fact that novel shapes with performance comparable to known optimal shapes were obtained from the ML models-based optimization process is a validation of the effectiveness this approach of using ML model surrogates in the design optimization process.

Table 3. ML model predictions versus simulation results on raw and regular shapes.

Objective function	Parameter	Range with ML models over several shapes (raw)	Mean with ML models over several shapes (raw)	ML model (regular)	Simulation (regular)
fRe	*fRe*	6.60-9.20	7.49	14.11	9.24
Nu$_{H1}$/fRe	*Nu$_{H1}$*	4.13-4.23	4.18	3.91	4.08
	fRe	10.70-14.95	12.07	15.35	14.87
	Nu$_{H1}$/fRe	0.29-0.39	0.35	0.255	0.274
Nu$_{H2}$/fRe	*Nu$_{H2}$*	3.33-4.09	3.85	4.08	4.23
	fRe	10.41-14.53	11.72	11.08	15.90
	Nu$_{H2}$/fRe	0.23-0.38	0.33	0.368	0.266

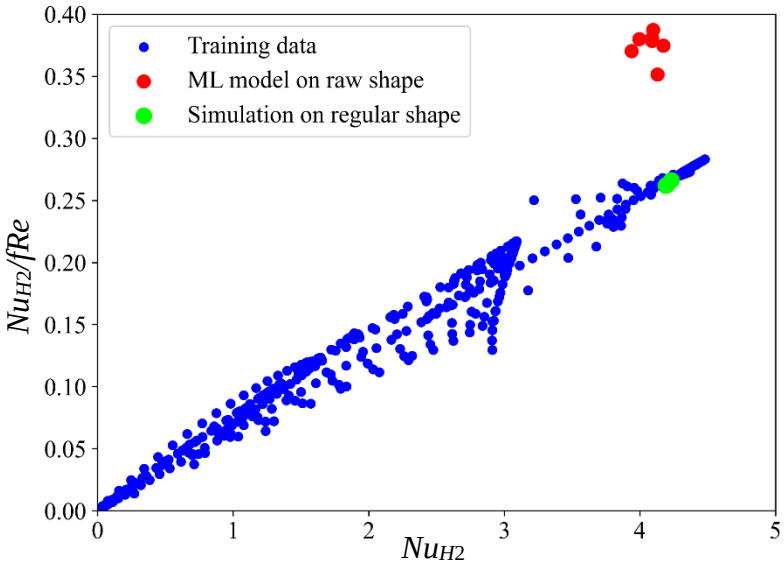

Figure 5. Comparison of *Nu$_{H2}$/fRe* values of the training data, ML model predictions for the raw shapes, and the numerical simulation predictions for the regular shapes.

4. Conclusion

ML-based surrogate models for *fRe*, Nu_{H1} and Nu_{H2} were developed using data collected from existing correlations, validated against data outside the dataset, and then used for optimizing flow cross-section shapes of constant cross-section channels. The trained ML models were found to have good prediction accuracy for shapes similar to those in the training dataset, but reduced performance on shapes highly dissimilar from the training data. For shapes in the training dataset, the mean percentage error was 0.70% for the *fRe* model, 1.24% for the Nu_{H1} model, and 2.84% for the Nu_{H2} model. Thus, the ML models do not serve as a universal correlation valid for any shapes, but rather, very effectively collapse all the known correlations into a single predictive correlation.

The ML surrogates are then used as the basis for optimization of the shape cross section based on performance metrics that aim to increase the Nusselt number and decrease the friction factor. The interior point method was identified as a suitable optimization method from quantitative assessment of four different numerical-derivative and non-derivative-based optimization algorithms. For each objective function explored, a novel shape was generated by the optimizer that was unique from the training data, namely, a three-lobed shaped duct to reduce the friction factor, and a pentagon with rounded sides and an ice-cream cone like shape for different area goodness-based metrics. Finite volume simulations were run on post-processed versions of the raw optimized shapes to make them more regular, and the results were compared to the predictions by the ML models. The ML model predictions of Nusselt number were generally found to be more accurate than predictions of friction factors. However, the ML model predictions were shown to follow the correct trends with parametric variations of different shapes, due to which the surrogate model-based optimization processes were able to predict novel optimized shapes with performance as good as (if not slightly better than) currently known optimal shapes. Expectedly, shapes having outlying performance improvement far better than currently known optimal shapes were not identified, given that this relatively simple 2D design space has been exhaustively explored. Nevertheless, the identification of novel optimized shapes with performance comparable to known optimal shapes is a validation of the optimization capabilities of the ML-assisted optimization process.

When using these ML models, it is important to ensure that the area enclosed within the shape is normalized to 1 square unit. To further improve accuracy of the predictions, it is recommended that the average value of predictions for several rotational orientations of the shape is used as the final prediction. When using the ML models on shapes belonging to classes

outside the training set, numerical simulations should always be carried out for confirmation of the exact *Nu* and *fRe* values.

The use of ML-based surrogate models in the design optimization framework holds promise and should be explored further. This method could be extended from simple 2D geometry optimization to 3D systems with the training and availability of ML-based *fRe* and *Nu* surrogate models. The advantages of using ML models for design optimization are anticipated to increase with increased complexity of the system. In the case of such complex systems, the computational advantage of using ML-model-based optimization approaches versus iterative numerical simulations will also be significant.

Acknowledgement

Financial support for this work provided by members of the Cooling Technologies Research Center, a graduated National Science Foundation Industry/University Cooperative Research Center at Purdue University, is gratefully acknowledged. The authors acknowledge the use of the MATLAB script GA550.m from the Multidisciplinary Design Optimization course taught at Purdue University by Prof. William Crossley.

References

[1] F. Chollet, Deep learning with Python, 2nd ed., Manning, 2021.
[2] F.E. Bock, R.C. Aydin, C.J. Cyron, N. Huber, S.R. Kalidindi, B. Klusemann, A review of the application of machine learning and data mining approaches in continuum materials mechanics, Front. Mater. 6 (2019) 1–23.
[3] S. Nasiri, M.R. Khosravani, K. Weinberg, Fracture mechanics and mechanical fault detection by artificial intelligence methods: A review, Eng. Fail. Anal. 81 (2017) 270–293.
[4] S.L. Brunton, B.R. Noack, P. Koumoutsakos, Machine learning for fluid mechanics, Annu. Rev. Fluid Mech. 52 (2020) 477–508.
[5] H. Ganti, P. Khare, Data-driven surrogate modeling of multiphase flows using machine learning techniques, Comput. Fluids. 211 (2020) 104626.
[6] A. Mosavi, M. Salimi, S.F. Ardabili, T. Rabczuk, S. Shamshirband, A.R. Varkonyi-Koczy, State of the art of machine learning models in energy systems, a systematic review, Energies. 12 (2019).
[7] K. Amasyali, N.M. El-Gohary, A review of data-driven building energy consumption prediction studies, Renew. Sustain. Energy Rev. 81 (2018) 1192–1205.
[8] H. Ghoddusi, G.G. Creamer, N. Rafizadeh, Machine learning in energy economics and finance: A review, Energy Econ. 81 (2019) 709–727.
[9] S. Seyedzadeh, F.P. Rahimian, I. Glesk, M. Roper, Machine learning for estimation of building energy consumption and performance: a review, Vis. Eng. 6 (2018).
[10] C. Voyant, G. Notton, S. Kalogirou, M.L. Nivet, C. Paoli, F. Motte, A. Fouilloy, Machine learning methods for solar radiation forecasting: A review, Renew. Energy. 105 (2017) 569–582.
[11] A. Maleki, A. Haghighi, I. Mahariq, Machine learning-based approaches for modeling thermophysical properties of hybrid nanofluids: A comprehensive review, J. Mol. Liq. 322

(2021).
[12] T. Ma, Z. Guo, M. Lin, Q. Wang, Recent trends on nanofluid heat transfer machine learning research applied to renewable energy, Renew. Sustain. Energy Rev. 138 (2021) 1–16.
[13] S.S. Pai, A. Banthiya, Transfer-learning-based surrogate model for thermal conductivity of nanofluids, ArXiv. preprint (2022) 1–20.
[14] Y. Qiu, D. Garg, L. Zhou, C.R. Kharangate, S.M. Kim, I. Mudawar, An artificial neural network model to predict mini/micro-channels saturated flow boiling heat transfer coefficient based on universal consolidated data, Int. J. Heat Mass Transf. 149 (2020) 119211.
[15] L. Zhou, D. Garg, Y. Qiu, S.M. Kim, I. Mudawar, C.R. Kharangate, Machine learning algorithms to predict flow condensation heat transfer coefficient in mini/micro-channel utilizing universal data, Int. J. Heat Mass Transf. 162 (2020) 120351.
[16] G. Zhu, T. Wen, D. Zhang, Machine learning based approach for the prediction of flow boiling/condensation heat transfer performance in mini channels with serrated fins, Int. J. Heat Mass Transf. 166 (2021) 120783.
[17] Y. Suh, R. Bostanabad, Y. Won, Deep learning predicts boiling heat transfer, Sci. Rep. 11 (2021) 1–10.
[18] G.M. Hobold, A.K. da Silva, Visualization-based nucleate boiling heat flux quantification using machine learning, Int. J. Heat Mass Transf. 134 (2019) 511–520.
[19] A. Parrales, A. Hern, O. Flores, H. Hernandez, Heat transfer coefficients analysis in a helical double-pipe evaporator: Nusselt number correlations through artificial neural networks, Entropy. 21 (2019) 1–14.
[20] R. Beigzadeh, M. Rahimi, Prediction of heat transfer and flow characteristics in helically coiled tubes using artificial neural networks, Int. Commun. Heat Mass Transf. 39 (2012) 1279–1285.
[21] G.N. Xie, Q.W. Wang, M. Zeng, L.Q. Luo, Heat transfer analysis for shell-and-tube heat exchangers with experimental data by artificial neural networks approach, Appl. Therm. Eng. 27 (2007) 1096–1104.
[22] G. Xie, B. Sunden, Q. Wang, L. Tang, Performance predictions of laminar and turbulent heat transfer and fluid flow of heat exchangers having large tube-diameter and large tube-row by artificial neural networks, Int. J. Heat Mass Transf. 52 (2009) 2484–2497.
[23] R. Beigzadeh, M. Rahimi, O. Jafari, A.A. Alsairafi, Computational fluid dynamics assists the artificial neural network and genetic algorithm approaches for thermal and flow modeling of air-forced convection on interrupted plate fins, Numer. Heat Transf. Part A Appl. 70 (2016) 546–565.
[24] J.K. Ostanek, Improving pin-fin heat transfer predictions using artificial neural networks, in: Vol. 3A Heat Transf., American Society of Mechanical Engineers, 2013.
[25] S. Chokphoemphun, S. Hongkong, S. Thongdaeng, S. Chokphoemphun, Experimental study and neural networks prediction on thermal performance assessment of grooved channel air heater, Int. J. Heat Mass Transf. 163 (2020) 120397.
[26] Y. Islamoglu, A. Kurt, Heat transfer analysis using ANNs with experimental data for air flowing in corrugated channels, Int. J. Heat Mass Transf. 47 (2004) 1361–1365.
[27] B. Kwon, F. Ejaz, L.K. Hwang, Machine learning for heat transfer correlations, Int. Commun. Heat Mass Transf. 116 (2020) 104694.
[28] A. Barron, Approximation and estimation bounds for artificial neural networks, Mach. Learn. 14 (1994) 115–133.
[29] S.S. Pai, D. Visaria, J.A. Weibel, A machine-learning-based surrogate model for internal flow nusselt number and friction factor in various channel cross sections, 20th IEEE Intersoc. Conf. Therm. Thermomechanical Phenom. Electron. Syst. (2021) 1024–1029.
[30] R.K. Shah, A.L. London, Laminar flow forced convection in ducts: a source book for compact heat exchanger analytical data, 2014.
[31] M. Spiga, G.L. Morini, Nusselt numbers in laminar flow for H2 boundary conditions, Int. J. Heat Mass Transf. 39 (1996) 1165–1174.
[32] S.S. Pai, J.A. Weibel, ML-based Surrogate Models for Nusselt Number and Friction Factor Prediction in Constant Cross-Section Channels, https://nanohub.org/resources/mlmodels2d, (2022). DOI: 10.21981/0MJE-TQ48.